RSC Advances

ROYAL SOCIETY OF CHEMISTRY

www.rsc.org/advances

Cite this: DOI: 10.1039/c0xx00000x

www.rsc.org/xxxxxx

ARTICLE TYPE

Glucose-assisted hydrothermal synthesis of few-layer reduced graphene oxide wrapped mesoporous TiO_2 submicrospheres with enhanced electrochemical performance for lithium-ion batteries

Jun Peng[a] , Gang Wang[a*], Yong-Tao Zuo[a], Gang Li[a], Feng Yu[a*], Bin Dai[a], Xu-Hong Guo[a,b]

Received (in XXX, XXX) Xth XXXXXXXXX 20XX, Accepted Xth XXXXXXXXX 20XX
DOI: 10.1039/b000000x

A facile and green strategy for the synthesis of few-layer reduced graphene oxide (FL-RGO)-wrapped mesoporous anatase TiO_2 (m-TiO_2) submicrospheres (denoted as m-TiO_2@FL-RGO) composite was developed via glucose-assisted hydrothermal GO reduction and TiO_2 crystallization. In this approach, glucose is important for tighly immobilizing FL-RGO on the surface of m-TiO_2 submicrospheres. The wrapping of FL-RGO improves the electrochemical kinetics of the m-TiO_2 submicrospheres, which results in superior electrochemical performance in terms of specific capacity, rate capability and cycle stability. The material shows a discharge capacity of 202.5 mA h g^{-1} at 0.6C after 100 cycles. Even at a current rate of 30C, a high discharge capacity of 113.5 mAh g^{-1} is still obtained, which is two-fold higher than that of pristine m-TiO_2 submicrospheres. The superior electrochemical performance offered by the m-TiO_2@FL-RGO composite is attributed to the enhanced electronic conductivity due to the graphene wrapping and effective diffusion of Li ions in the interconnected network of nanoparticles forming the mesoporous anatase TiO_2 submicrospheres.

[a] *School of Chemistry and Chemical Engineering, Key Laboratory for Green Processing of Chemical Engineering of Xinjiang Bingtuan, Shihezi University, Shihezi, P.R. China. E-mail:gwangshzu@163.com (G. Wang) and yufeng05@mail.ipc.ac.cn (F. Yu).*

[b] *State Key Laboratory of Chemical Engineering, East China University of Science and Technology, Shanghai 200237, P. R. China*

Cite this: DOI: 10.1039/c0xx00000x

www.rsc.org/xxxxxx

ARTICLE TYPE

1. Introduction

Rechargeable Li-ion batteries (LIBs) are now widely considered the most important power sources for various portable electronic devices, electric vehicles (EVs) and hybrid electronic vehicles (HEVs).[1-4] However, commercial Li-ion batteries still cannot satisfy the requirements of those large-scale power sources. They encounter the necessity of breakthroughs in terms of power/energy densities, safety, and long-term stability.[5,6] Although graphite is most commonly used as an anode, it has serious safety problems including dendritic growth of Li due to the low operating voltage (~0.2 V vs. Li/Li^+).[7-9] As a result, numerous efforts have been devoted to developing safe, high-performance transition-metal oxide anode materials.[10-12] In this respect, TiO_2 has attracted significant attention because of its relatively high lithium insertion/extraction voltage (~1.6V vs. Li/Li^+) that can efficiently avoid the formation of solid electrolyte interface (SEI) layers and lithium plating on the anode. This improves the safety of the batteries versus traditional graphite anodes.[13-17] In addition, its low volume variation (<4%) during the lithiation/delithiation process favors large-scale energy storage.[15] Unfortunately, TiO_2 has poor electronic and ionic conductivity that limits its application as a high power anode material.

Constructing mesoporous architecture in the material is an appealing strategy currently used to improve rate performance.[18-23] Mesoporous TiO_2 with a high surface area can provide more active surface sites and electrolyte-electrode interface and a short diffusion distance for Li^+ ions. This promotes fast and reversible lithium insertion and extraction.[18,20,23-29] In particular, spherical mesoporous TiO_2 particles with a submicrometer size have an ideal morphology for conventional electrode fabrication because these spherical mesoporous TiO_2 particles have a high packing density, less agglomeration, and good particle mobility to form a compact electrode layer.[18,22,28-30] However, the large particle sizes on a scale of micrometers increases the transport distance of electrons in these submicrometer particles. This greatly impairs the performance of mesoporous TiO_2. To enhance electron transport, carbonaceous material coatings are commonly applied.[31,32]

Graphene nanosheets are a new 2D carbon nanomaterial. They are particularly promising for improving the electrochemical performances of various electrode materials due to their superior electrical conductivity, large surface area, and excellent structural flexibility versus conventional carbonaceous materials.[33] Various graphene-TiO_2 hybrid materials exhibiting enhanced electrochemical properties have been intensively reported.[8,15,34-37] However, creating an uniform coating of grapnene on mesoporous microspheres is still challenging. Recently, Yan et al. synthesized reduced graphene oxide wrapped mesoporous TiO_2 microspheres via a UV-assisted photocatalytic method. The material shows a discharge capacity of 155.8 mAh g^{-1} at the 5 C rate. Even at the 60 C rate, there was still a high discharge capacity of 83.6 mAh g^{-1}. This is two times higher than that of pristine mesoporous TiO_2.[38] Chen et al. report a rational design of graphene sheets-wrapped anatase TiO_2 hollow particles. The graphene-wrapped TiO_2 hollow particles exhibit significantly enhanced lithium storage capabilities versus the pure TiO_2 counterpart.[39] Although the electrochemical performance of TiO_2/graphene composites can be remarkably improved in these cases, the synthetic routes, however, involve toxic functional reagents (such as 3-aminopropyltrimethoxysilane) and relatively complicated experimental procedures. This limits the practical applications. A key challenge in this strategy is the achievement of both high electrical conductivity and a low-weight fraction of thin graphene layers on the surface of mesoporous microspheres. Thus, it is very important to develop a facile and green approach for the synthesis of graphene-wrapped TiO_2 composites with favored structures for high-performance LIBs.

Herein, we describe a novel and green strategy for the synthesis of few-layer reduced graphene oxide (FL-RGO)-wrapped mesoporous anatase TiO_2 (m-TiO_2) submicrospheres (denoted as m-TiO_2@FL-RGO) composite through glucose-assisted hydrothermal GO reduction and TiO_2 crystallization. During the hydrothermal process, glucose serves as a reducer and linker between GO and FL-RGO. It immobilizes FL-RGO on the surface of the m-TiO_2 submicrospheres. Such composite with a hierarchical core/shell structure are advantageous for enhancing the electronic conductivity among the mesoporous anatase submicrospheres and offer a short pathway for Li^+ diffusion within the mesoporous anatase submicrospheres. Specifically, the m-TiO_2@FL-RGO composite delivers highly reversible capacities with superior cyclic capacity retention for prolonged cycling and presenting excellent high-rate capability at a current rate of 30C, this suggests that the material has great potential as a high-rate anode material for lithium storage.

2. Experimental section

2.1 Materials and methods

Natural graphite powder (325 mesh) was purchased from Alfa-Aesar. Potassium chloride (KCl), tetrabutyl titanate (TBT), and glucose were purchased from Adamas Reagent (Shanghai, China). Graphene oxide (GO) was synthesized from graphite powder according to the modified Hummers method.[40,41]

Synthesis of m-TiO_2@FL-RGO composite: Amorphous TiO_2 submicrospheres were prepared via a sol-gel process using tetrabutyl titanate as a precursor according to the literatures.[42,43] To wrap GO on the surface of the amorphous TiO_2 submicrospheres, amorphous TiO_2 submicrospheres (0.08 g) were first dispersed in dilute HCl (0.02 M, 20 mL) via sonication. After 30 min, the TiO_2 dispersion (4 mg mL^{-1}) was added into a 20 mL aqueous graphene oxide suspension (0.2 mg mL^{-1}) and glucose (0.02 g) was added under mild magnetic stirring. After 1h,

the mixed suspension was transferred into a Teflon-sealed

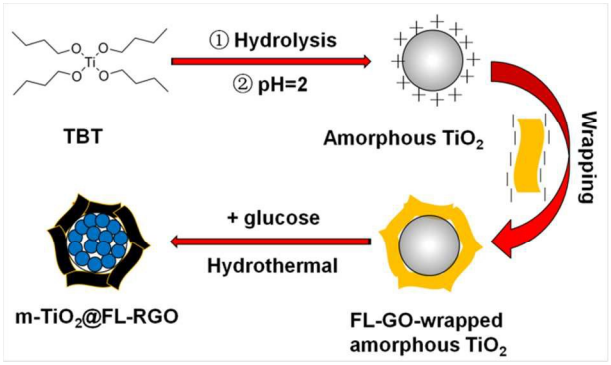

Scheme 1 The formation of the m-TiO_2@FL-RGO composite.

autoclave and maintained at 180 °C for 16 h. For comparison, m-TiO_2 submicrospheres were obtained using the above-mentioned mothed without GO and glucose added. The final precipitates were collected and thoroughly washed with distilled water and absolute alcohol, and finally calcined at 400 °C for 2 h in an argon atmosphere to obtain highly crystalline samples. The actual amounts of RGO in the m-TiO_2@FL-RGO composite were estimated from carbon contents (wt %) by elemental analysis: 4.8 wt.% .

2.2. Materials characterization

X-ray diffraction (XRD) of the samples was measured on a Bruker AXS D8 X-ray diffractometer with a Cu-Ka X-ray source operating at 40 kV and 100 mA. The morphologies of the materials were observed using field-emission scanning electron microscope (FESEM, JEOL JSM-6700F) and a transmission electron microscope (TEM, FEI Tecnai G2). The Raman spectra of the samples were measured at room temperature using a ViaReflex Raman spectrometer at 514 nm excitation. Nitrogen adsorption and desorption isotherms were measured at 77 K on a Micromeritics ASAP2010 instrument. Specific surface area calculations were made using the Brunauer–Emmett–Teller (BET) method. The poresize distribution (PSD) curves were calculated from the isotherm using the BJH (Barrett–Joyner–Halenda) algorithm. The relative compositions of graphene were measured using a CHNS analyzer (Flash EA 1112).

2.3. Electrochemical characterization

The electrochemical experiments were performed using 2032-type coin cells; metallic lithium foil served as the counter electrode. The working electrodes were prepared with active materials, carbon black, and PVDF binder at a weight ratio of 8:1:1 in N-methyl-2-pyrrolidinone (NMP). The obtained slurry was coated onto Cu foil and dried at 120℃ for 12h. The dried tape was then punched into round plates with a diameter of 12.0 mm as the cathode electrodes. The loading density of the electrode was about 2 mg cm^{-2}. The working electrode and counter electrode were separated by a Celgard 2400 membrane. The electrolyte was 1 M LiPF6 dissolved in a mixture of ethyl carbonate (EC), dimethyl carbonate (DMC) and ethylmethyl carbonate (EMC) at a volume ratio of 1:1:1. Galvonostatic charge–discharge was measured on a LAND (Wuhan, China) battery tester in the voltage window of 1.0–3.0 V versus Li/Li^+. Cyclic voltammetry (CV) and electrochemical impedance spectroscopy (EIS) were measured using a potentiostat (CHI

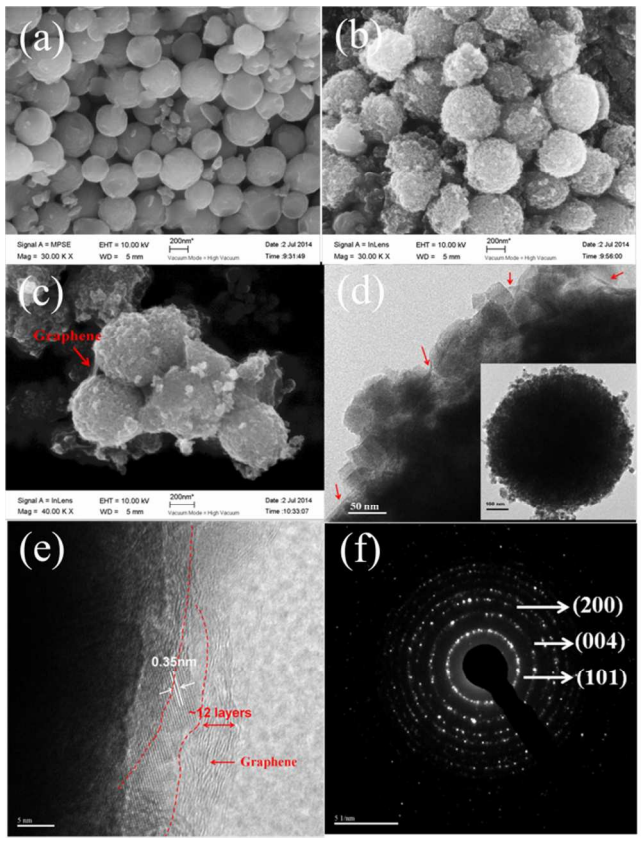

Fig. 1 FE-SEM images of (a) amorphous TiO_2 submicrospheres, (b) m-TiO_2 submicrospheres and (c) m-TiO_2@FL-RGO composite, and TEM and HRTEM image (d, e and f) of m-TiO_2@FL-RGO composite.

604C, CH Instrumental Inc.). The impedance spectra were recorded by applying an AC voltage of 5 mV from 100 kHz to10 mHz.

3. Results and discussion

The synthesis strategy for the m-TiO_2@FL-RGO composite is schematically depicted in Scheme 1. First, the amorphous TiO_2 submicrospheres that absorbed lots of the hydroxyl groups (-OH) on the surface were synthesized through a controlled hydrolysis of TBT.[42,43] Under the acidic environment, the surface of amorphous TiO_2 submicrospheres was positively charged due to the protonation effect of the hydroxyl groups, while the surface of the graphene oxide was negatively charged because of the ionization of the carboxylic acid and phenolic hydroxy groups.[44,45] Their zeta potentials under the specified conditions were showed in Table S1. The amorphous TiO_2 submicrospheres were then assembled with negatively charged graphene oxide via electrostatic interactions. This was easily triggered when TiO_2 and graphene oxide were oppositely charged. Finally, the resulting aggregates were chemically reduced via a glucose-assisted hydrothermal treatment to form a m-TiO_2@FL-RGO composite. In this way, glucose not only reduces GO to FL-RGO,[46,47] but is also a linker to prevent the exfoliation of RGO from the surface of m-TiO_2 submicrospheres during hydrothermal reduction.[47]

The morphology and microstructure of the m-TiO_2@FL-RGO composite were examined by SEM, TEM and high-resolution TEM (HRTEM). For comparison, SEM of amorphous TiO_2 submicrospheres and mesoporous TiO_2 submicrospheres were also observed. From SEM images, one can find that smooth, amorphous TiO_2 submicrospheres with an average diameter of 500 nm were obtained via a sol-gel process (Fig. 1a). After hydrothermal treatment for the crystallization of amorphous TiO_2 submicrospheres, mesoporous TiO_2 submicrospheres were obtained (Fig. 1b). The SEM image in Figure 1b indicates that these TiO_2 submicrospheres are actually composed of small particles leading to a relatively rough surface. For the m-TiO_2@FL-RGO composite, the RGO can be easily identified as the thin sheets that ''wrap'' around these TiO_2 submicrospheres and also bridge nearby particles together (Fig. 1c). Fig. 1d shows a typical TEM image of the as prepared m-TiO_2@FL-RGO composite. It can be seen that the m-TiO_2@FL-RGO composite still kept a sphere-like morphology. Due to the low contrast of RGO, it hardly be viewed under a low magnification (Fig. 1d, indicated by red arrows). A further HRTEM image in Fig. 1e confirms that the few-layered graphene nanosheets (~12 layers) indeed wrap around the TiO_2 submicrospheres. Furthermore, the HRTEM image shows a well-defined crystallinity of TiO_2 with a lattice spacing of 0.35 nm, which is assigned to the (101) plane of anatase. The selected-area electron diffraction (SAED) pattern (Fig. 1f) with diffraction rings (101), (004) and (200) of randomly oriented anatase TiO_2 further confirms its high crystallinity.

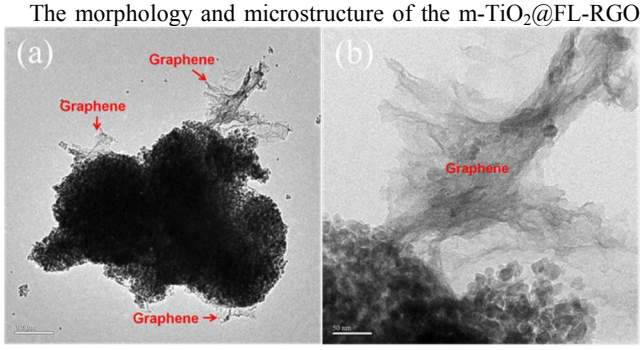

Fig. 2 TEM images of the m-TiO_2@FL-RGO synthesized in the absence of glucose.

To investigate the role of glucose during a hydrothermal treatment, m-TiO_2@FL-RGO composites in the absence of glucose were also synthesized (using a similar strategy). The corresponding TEM images are shown in Fig. 2 and Fig. S1. Compared with the m-TiO_2@FL-RGO composite synthesized in the presence of glucose (Fig. 1d and 1e), there is an obvious exfoliation of RGO from the surface of m-TiO_2 submicrospheres in Fig. 2 and Fig. S1. This indicates that the presence of glucose can immobilize the RGO on the surface of m-TiO_2 submicrospheres and facilitates the wrapping of RGO nanosheets on the surface of m-TiO_2 submicrospheres.

XRD patterns of amorphous TiO_2 submicrospheres, m-TiO_2 submicrospheres, and m-TiO_2@FL-RGO composite are shown in Fig. 3a. No peak was observed in the XRD patterns of amorphous TiO_2 submicrospheres, indicating that the pre-formed TiO_2 submicrospheres were amorphous, while all the identified peaks for m-TiO_2 submicrospheres and m-TiO_2@FL-RGO composite were assigned to anatase (JCPDS, no. 21-1272). Note that the diffraction peak corresponding to graphene was not observed in the XRD pattern of m-TiO_2@FL-RGO composite due to the strong intensities of diffraction peaks from crystalline TiO_2 submicrospheres. In addition, the broad diffraction peaks of TiO_2 for m-TiO_2 submicrospheres and m-TiO_2@FL-RGO composite suggest a small crystalline size. According to the Scherrer equation ($D = K\lambda/\beta\cos\theta$), the crystallite size, calculated from the (101) reflection of TiO_2, were similar for two samples and the average crystallite size is 9.2 nm, suggesting that the wrapping of FL-RGO does not influence the crystal structure of the host TiO_2 material.

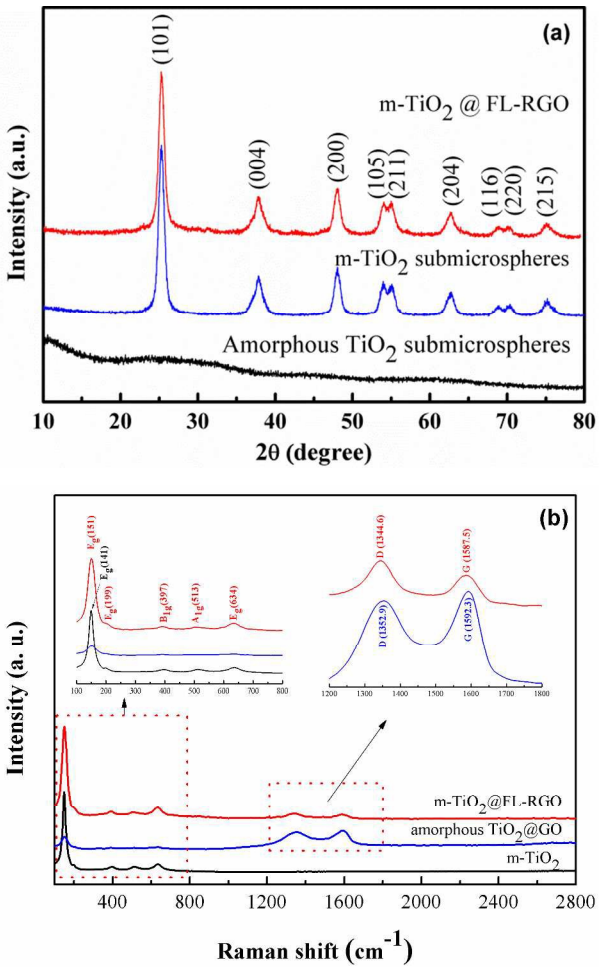

Fig.3 (a) XRD patterns of the amorphous TiO_2 submicrospheres, m-TiO_2 submicrospheres and m-TiO_2@FL-RGO composite; (b) Raman spectra of m-TiO_2 submicrospheres, amorphous TiO_2@GO and m-TiO_2@FL-RGO composite.

The chemical composition of the m-TiO_2@FL-RGO composite was also confirmed by analysis of Raman spectrum. Fig. 3b compares the Raman spectrum of the m-TiO_2 submicrospheres, amorphous TiO_2@GO and m-TiO_2@FL-RGO composite. In the Raman spectrum of m-TiO_2 submicrospheres and m-TiO_2@FL-RGO composite, the characteristic peak of 151 cm^{-1} observed for m-TiO_2@FL-RGO composite is attributed to the anatase E_g mode at 141 cm^{-1} of m-TiO_2 submicrospheres. The shift towards high frequency is caused by the interaction of TiO_2 with graphene.[48,49] Besides these Raman modes of anatase phase TiO_2, the Raman bands at 1344.6 and 1587.5 cm^{-1} for m-TiO_2@FL-RGO

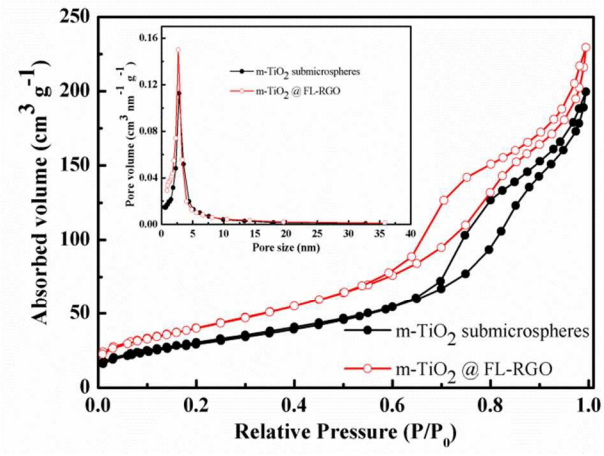

Fig. 4 Nitrogen adsorption–desorption isotherm curves and pore size distribution of m-TiO_2 submicrospheres and m-TiO_2@FL-RGO composite

composite, denoted as the D line (breathing mode of k-point phonons of A_{1g} symmetry) and the G line (the first-order scattering of the E_{2g} phonons), are also observed. The D- and G-bands of the amorphous TiO_2@GO located at 1352.9 and 1592.3 cm^{-1}, respectively. This indicates the successfully reduction of GO after hydrothermal treatment. In addition, the increase of the intensity ratio of D/G bands from 0.88 to 1.02 after hydrothermal treatment further confirms the reduction of GO.

The specific surface area and pore size distribution of the samples were further investigated by nitrogen adsorption–desorption isotherms. As shown in Fig. 4a, both samples have an IV-type isotherm curve with a distinct hysteresis loop in the range from 0.6~1.0 P/P_0, which is indicative of mesoporous materials. The pore size distribution plots are calculated from the desorption isotherm using the Barrett–Joyner–Halenda (BJH) model and are presented in Fig. 4b. Both samples show uniform mesopores with an average pore diameter of 3.5 nm. This indicates that RGO does not affect the mesoporous property of the TiO_2 microspheres. The standard multipoint Brunauer–Emmett–Teller (BET) method was used to calculate the specific surface area of the materials. It shows that the specific surface area of the m-TiO_2 submicrospheres is 146.3 m^2 g^{-1}. The m-TiO_2@FL-RGO composite possesses a higher specific surface area of 158.4 m^2 g^{-1}, which may be attributed to the contribution of FL-RGO. The high surface area in association with its mesoporous features facilitates faster lithium-ion diffusion due to efficient contact between active materials and electrolytes in the electrochemical reactions, thereby improving the electrochemical performance in LIBs.

The electrochemical properties were investigated systematically using 2032 coin-type cells in which a lithium foil served as both the counter and reference electrode. Fig. 5 compares the cyclic voltammograms (CVs) of m-TiO_2 submicrospheres and m-TiO_2@FL-RGO composite cycled within a voltage range of 1.0–2.5 V (vs Li/Li^+) at a scan rate of 0.1 mV s^{-1}. Both samples exhibit similar CV patterns. Consistent with previous studies,[50-53] two redox current peaks are observed at ~1.6 and ~2.2 V (vs Li/Li^+) during the cathodic and anodic scans, respectively. These two peaks reflect the insertion/removal processes of lithium ions as they move in and out of the anatase framework. There are small deviations in the peak positions for

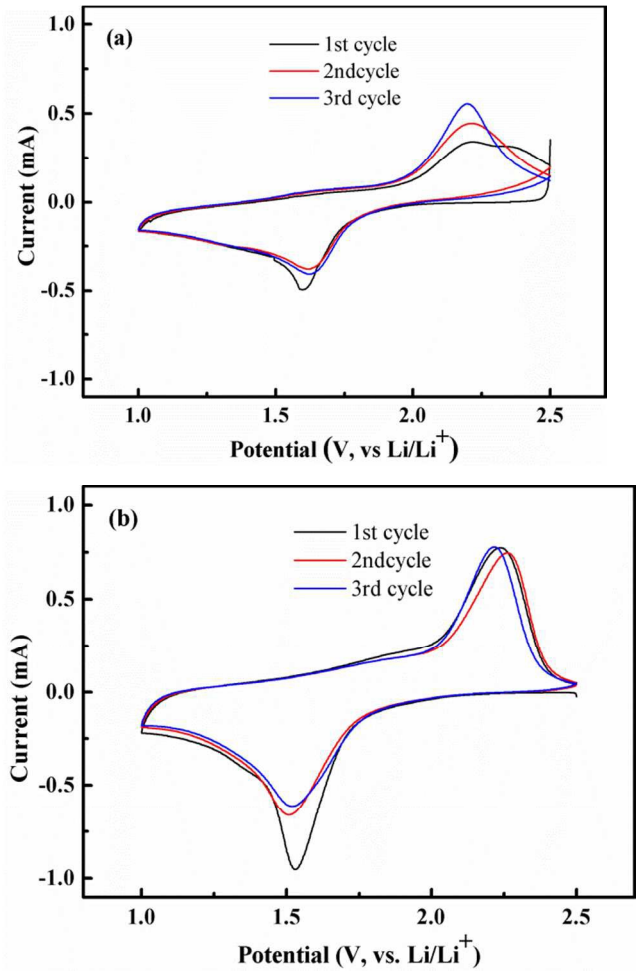

Fig. 5 Cyclic voltammograms of (a) m-TiO_2 submicrospheres and (b) m-TiO_2@FL-RGO composite cycled between 1.0 and 2.5 V (vs Li/Li^+) at a scan rate of 0.1 mV s^{-1}.

two electrodes in the subsequent cycles indicating the possible existence of a structural rearrangement of the TiO_2 crystal lattice.[51] There are, however, some noticeable differences between these two profiles. The anodic peak current increased slightly for m-TiO_2 submicrospheres during subsequent scans. This suggests an irreversible activation process in the electrode material. On the contrary, there are no substantial changes in the current for m-TiO_2@FL-RGO composite, indicating that the electrochemical reactions are more reversible in the latter case.

The lithium-storage properties of m-TiO_2 submicrospheres and m-TiO_2@FL-RGO composite were investigated by galvanostatic discharge–charge measurements. Fig. 6a and b shows the 1st, 2nd, 5th, 20th and 50th discharge and charge profiles of m-TiO_2 submicrospheres and m-TiO_2@FL-RGO composite in the voltage window of 1.0–3.0 V (vs Li/Li^+) at about 0.6C (1C = 168 mA g^{-1}, for 0.5 Li^+ insertion/extraction into/from TiO_2). In agreement with the above CV analysis, the initial charge–discharge voltage profiles of both electrodes look quite similar. Two distinct voltage plateaus at ~1.7 and ~2.0 V (vs Li/Li^+) can be observed during the initial discharge and charge processes. This confirms that the Li insertion takes place via a characteristic two-phase

reaction mechanism of anatase TiO_2. The lithium insertion process can be divided into three different domains from the

Cite this: DOI: 10.1039/c0xx00000x

www.rsc.org/xxxxxx

ARTICLE TYPE

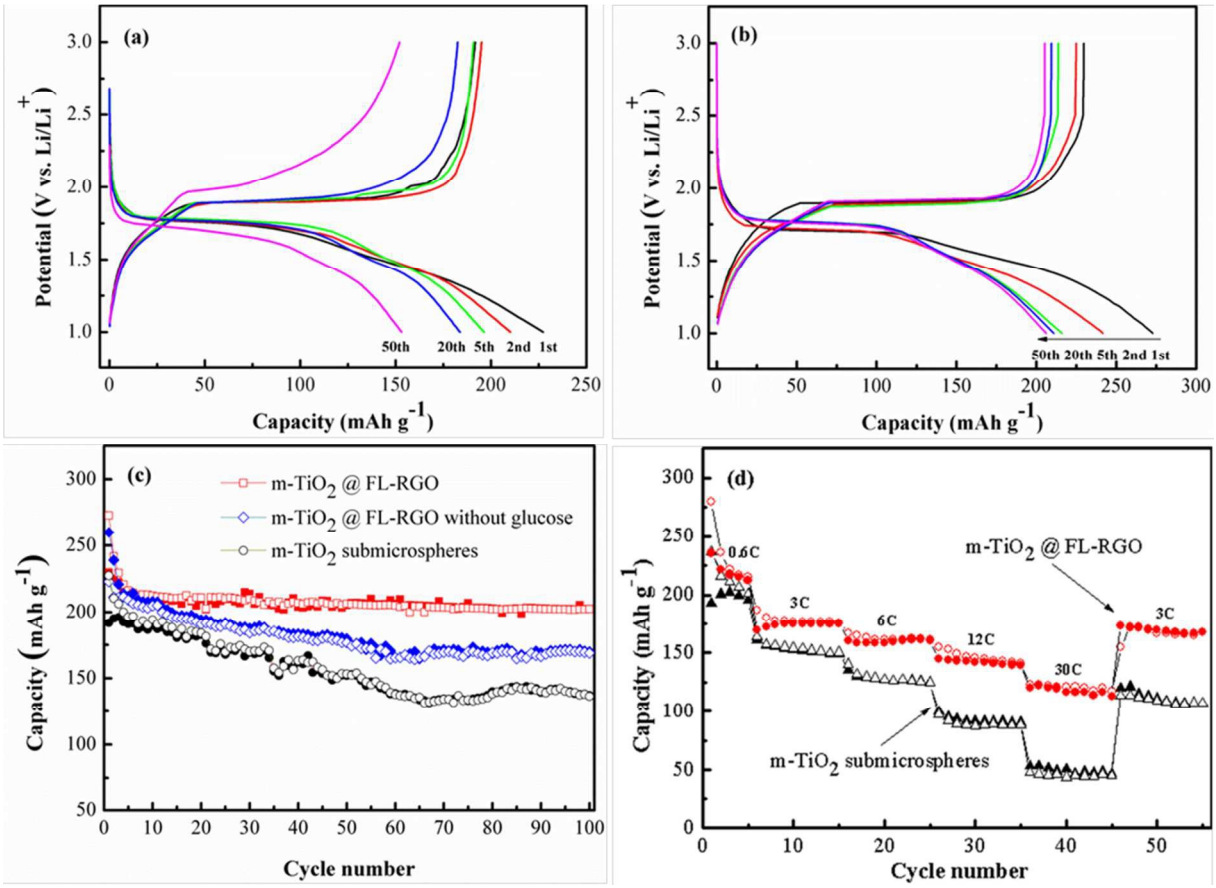

Fig. 6 Galvanostatic discharge–charge curves of (a) m-TiO_2 submicrospheres and (b) m-TiO_2@FL-RGO composite cycled at the 1st, 2nd, 5th, 20th, and 50th between 1.0 and 3 V (vs Li/Li^+) at 0.6C; (c) Cycling stability of m-TiO_2 submicrospheres and m-TiO_2@FL-RGO composite at 0.6C; (d) Rate performance of m-TiO_2 submicrospheres and m-TiO_2@FL-RGO composite at various current densities between 0.6C and 30C.

discharge curves. The first domain is marked by a fast potential drop starting from the open-circuit potential (about 2.4 V (vs Li/Li^+)) to ~1.7 V (vs Li/Li^+) due to a solid solution insertion mechanism. The second domain is characterized by a horizontal plateau region at ~1.7 V (vs Li/Li^+). This is a signature of a two-phase electrochemical reaction between a Li-poor phase and a Li-rich phase and reflects lithium insertion into vacancy sites of the TiO_2 crystal structure. The final domain is the long terminal voltage slope after the plateau region. This indicates further insertion of the lithium ions into the surface layer of the electrode material. Similar voltage profiles have been reported previously for anatase and TiO_2-graphene hybrid materials in the literature.[38,49,51,53,54] The initial discharge and charge capacities are 227 and 191.7 mAh g^{-1} for m-TiO_2 submicrospheres, and 272.8 and 229.7 mAh g^{-1} for m-TiO_2@FL-RGO composite, respectively. This led to an irreversible capacity loss of ~15.5% and ~15.8%, respectively. The large irreversible capacity for the two electrodes are due to the Li^+ storage in the irreversible sites and the decomposition of the electrolyte caused by adsorbed moisture in the mesoporous samples.[38,55] In addition, the reduction of oxygenated functional groups on the FL-RGO for the m-TiO_2@FL-RGO composite also gives rise to some irreversible capacity. From the second cycle, the m-TiO_2 submicrospheres electrode shows a rapidly capacity-fading along with a change in its voltage profile showing increased electrode polarization on cycling due to the intrinsically poor electronic conductivity, which has greatly undermined the value of the m-TiO_2 submicrospheres as anode materials for Li-ion batteries. On the contrary, the m-TiO_2@FL-RGO composite electrode shows almost superposed profiles that should be attributed to the higher electrochemical reactivity of the m-TiO_2@FL-RGO composite as well as excellent kinetics, indicating minimal capacity-fading and good reversibility. More importantly, the m-TiO_2@FL-RGO composite exhibits much better cycling performance than m-TiO_2 submicrospheres (Fig. 6c). The reversible capacity of the m-TiO_2@FL-RGO composite slightly decreases with cycling and reaches 202.5 mAh g^{-1} after 100 cycles, showing high capacity retention of 88.2%, while the reversible capacity of the m-TiO_2 submicrospheres decreases from 191.7 to only 137.1 mAh g^{-1} up

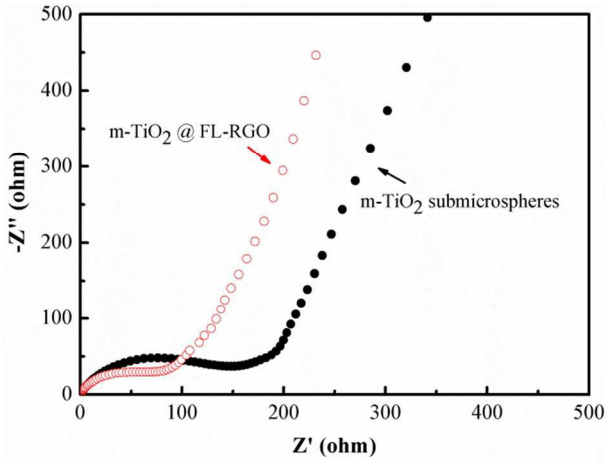

Fig. 7 Electrochemical impedance spectra of m-TiO_2 submicrospheres and m-TiO_2@FL-RGO composite.

to 100 cycles with only capacity retention rate of 71.5%. Meanwhile, the capacity of the m-TiO_2@FL-RGO composite synthesized in the absence of glucose is also exhibited in Fig. 6c. Due to the exfoliation of RGO from the surface of m-TiO_2 submicrospheres (see Fig. 2 and S1), this sample only delivers the reversible capacity of 168.9 mAh g^{-1} after 100 cycles, which is lower than that of the m-TiO_2@FL-RGO composite. In addition, the SEM of the m-TiO_2@FL-RGO composite electrode was also carried out to investigate the morphology and structural integrity of the electrode materials after 100 cycles at 0.6C (Figure S2 in the Supporting Information). As expected, the electrode is stable, and has no breakdown during the charging and discharging process. The overall spherical structures of the m-TiO_2@FL-RGO composite can be generally retained after 100 cycles. Therefore, the improved cycling stability for m-TiO_2@FL-RGO composite can be understood in terms of the intimate contact between the m-TiO_2submicrospheres and graphene wrapping layers, as well as the excellent structure stability of the materials.

High rate performance is one of the most significant electrochemical aspects of lithium-ion batteries for high-power applications such as HEV and EV. Fig. 6d compares the rate performance of the m-TiO_2 submicrospheres and m-TiO_2@FL-RGO composite under different current densities. With increasing current density from 0.6C to 30C, the discharge capacities of the two materials decrease, indicating the diffusion-controlled kinetics process for the electrode reaction. However, it is obvious that the reversible capacity of m-TiO_2@FL-RGO composite was held at 212.7 mAh g^{-1} after the 5th cycle at 0.6C. Upon increasing the discharge-charge rates to 3C, 6C, and 12C, the reversible capacities were maintained at about 175.3, 160.6 and 139.7 mAh g^{-1}, respectively. It was clear that all of the rate capacities of the m-TiO_2@FL-RGO composite were higher than those of the m-TiO_2 submicrospheres. Even at a high current density of 30C, the specific capacity remained at about 113.5 mAh g^{-1}, whereas that of the m-TiO_2 submicrospheres dropped to only 47.3 mAh g^{-1}. When the current rate was again reduced to 3C, the specific capacities of the m-TiO_2@FL-RGO composite returned to about 170 mAh g^{-1}, which did not ultimately change in the subsequent cycles. In addition, the LIB performance of bare RGO also was studied under the same test conditions to identify the capacity contribution from RGO. The result is consistent with the previous reports that bare RGO sheets show poor rate performance between 1.0 and 3.0 V (vs Li/Li^+) potential window (Fig. S3). Consider its content in the nanocomposite is about 4.8 wt.%, the capacity contribution from RGO can be neglected, especially at high rates. This further indicates that the improved lithium-insertion/extraction performance of m-TiO_2@FL-RGO composite can be due to high conductivity of graphene instead of its capacity contribution. We summarized the representative TiO_2/graphene composites for LIBs anode materials. Apparently, the rate performance of m-TiO_2@FL-RGO composite is superior to that of most of the previously reported TiO_2-graphene nanomaterials (see Table S2 in the Supporting Information).

In another study, we prepared m-TiO_2@RGO samples with different RGO contents by changing the starting concentration of GO in the hydrothermal process and studied their cycling performance at the charging/discharging rate of 6C (Table S3 and Fig. S4 in the Supporting Information). It is evident that the 4.8 wt.% graphene-wrapped m-TiO_2 exhibits 159.3 mA h g^{-1} at 6C after 100 cycles while the 2.2 wt.% graphene-wrapped m-TiO_2 sample is worse due to the insufficient amount of graphene for complete wrapping. However, too much of RGO (e.g. 8.4 wt.%) has little added electrochemical benefit—the thick graphene wrapping may inhibit the Li^+ diffusion. Graphene wrapping may has negative effects on the Li^+ diffusion due to the low Li-ion diffusivity (~10^{-11} cm^2 s^{-1}) through the perpendicular direction to the graphene layers. However, the highly conductive RGO wrapping in turn can accelerates the diffusion of Li^+ ions through a stronger internal electrical filed.[38] The key factor to influence the diffusion of Li^+ ions can depend on the wrapping thickness of graphene. A thin graphene wrapping should be more favorable for the diffusion of Li^+ ions. The optimum amount of graphene needs further study.

To understand the reasons for the improved high-rate performance, electrochemical impedance spectroscopy (EIS) measurements were carried out for m-TiO_2 submicrospheres and m-TiO_2@FL-RGO composite, and are presented in Fig. 7. The Nyquist plots for the two samples display a single semicircle in the high frequency region and a sloping straight line in the low frequency range. These correspond to charge-transfer resistance (R_{ct}) and solid-state diffusion of lithium in this insertion material (Z_W) respectively. Apparently, the radius of the semicircle of m-TiO_2@FL-RGO composite electrode is significantly smaller than that of m-TiO_2 submicrospheres electrode. This suggests that the charge transfer resistance of the m-TiO_2@FL-RGO composite is lower than that of m-TiO_2 submicrospheres. This confirmed that the wrapping of conductive graphene in the composite could facilitate the electron transfer from wrapped mesoporous anatase submicrospheres within the whole electrode. This effect contributes to the higher rate capability of m-TiO_2@FL-RGO composite electrode versus the m-TiO_2 submicrosphere electrode.

Based on the above observations, the outstanding electrochemical performance of the as-prepared m-TiO_2@FL-RGO as anode materials for LIBs can be understood from several perspectives. First, the mesoporous structure with high surface area provides more active surface sites and electrolyte-electrode interface than their solid counterparts. This results in a short diffusion distance for the Li^+ ions and promotes fast and reversible lithium insertion and extraction. Second, the RGO shell

provides strong interactions between the mesoporous TiO_2 and graphene. This allows efficient electron conduction among the mesoporous anatase submicrospheres and improves the electrochemical kinetics of the TiO_2 submicrospheres. Third, the robust core-shell structure with a submicrometer size effectively prevents the undesirable aggregation of conventional nanoparticles. This ensures the integrity of the electrode and improves the capacity retention upon prolonged cycling. In addition, the high crystallinity of the TiO_2 mesoporous spheres contribute to the electrical conductivity and crystal lattice robustness during repeated charge-discharge cycling. These features promote the electrochemical process and lead to high specific capacity—especially at high rates and cycling stability values.

4. Conclusions

The m-TiO_2@FL-RGO composite was synthesized by wrapping amorphous TiO_2 submicrospheres with GO followed by a one-step GO reduction and TiO_2 crystallization via glucose-assisted hydrothermal treatment. The m-TiO_2@FL-RGO composite had an excellent specific capacity of 202.5 mA h g^{-1} at 0.6C after 100 cycles. Even at a current density of 30C, there was still a high discharge capacity of 113.5 mA h g^{-1}. This is twice as high as pristine mesoporous TiO_2 submicrospheres. This improved rate capability was attributed to the enhanced electronic conductivity of mesoporous anatase submicrospheres via uniform graphene wrapping. We believe that this work is a powerful green route towards an effective wrapping of metal oxides with electron-conducting materials. This can enhance their electrochemical performance.

Acknowledgements

This work was financially supported by Program for Changjiang Scholars and Innovative Research Team in University (PCSIRT, No. IRT1161), Program of Science and Technology Innovation Team in Bingtuan (No 2011CC001), and the National Natural Science Foundation of China (No. 21263021, U1303291).

References

1 B. Kang and G. Ceder, Nature 2009, 458, 190.
2 J. B. Goodenough and Y. Kim, Chem. Mater., 2010, 22, 587.
3 V. Etacheri, R. Marom, R. Elazari, G. Salitra and D. Aurbach, Energy Environ. Sci., 2011, 4, 3243.
4 X. Hao and B. M. Bartlett, Adv. Energy Mater., 2013, 3, 753.
5 J. Cho, Y. J. Kim, T.-J. Kim and B. Park, Angew. Chem., Int. Ed., 2001, 40, 3367.
6 L. Hu, H. Zhong, X. Zheng, Y. Huang, P. Zhang and Q. Chen, Sci. Rep., 2012, 2, 986.
7 S. S. Zhang, K. Xu and T. R. Jow, J. Power Sources, 2006, 160, 1349.
8 S. B. Yang , X. L. Feng and K. Müllen, Adv. Mater., 2011, 23, 3575.
9 X. Li and C. Wang, J. Mater. Chem. A, 2013, 1, 165.
10 J. Wang, N. Yang, H. Tang, Z. Dong, Q. Jin, M. Yang, D. Kisailus, H. Zhao, Z. Tang and D. Wang, Angew. Chem., Int. Ed. 2013, 52, 6417.
11 P. Poizot, S. Laruelle, S. Grugeon, L. Dupont and J. M. Tarascon, Nature, 2000, 407, 496.
12 S. Yang, X. Feng, S. Ivanovici and K. Müllen, Angew. Chem., Int. Ed. 2010, 49, 8408.
13 G.-N. Zhu, Y.-G. Wang and Y.-Y. Xia, Energy Environ. Sci., 2012, 5, 6652.
14 Z. Wang and X.W. Lou, Adv. Mater., 2012, 24, 4124.
15 J. Qiu, P. Zhang, M. Ling, S. Li, P. Liu, H. Zhao and S. Zhang, ACS Appl. Mater. Interfaces, 2012, 4, 3636.
16 H. Kim, M.G. Kim, J. Cho, Adv. Energy Mater., 2012, 2, 1425.
17 R. Wang, X. Xue, W. Lu, H. Liu, C. Lai, K. Xi, Y. Che, J. Liu, S. Guo, D. Yang, Nanoscale, 2015, 7, 12833.
18 Y.-G. Guo, Y.-S. Hu and J. Maier, Chem. Commun., 2006, 26, 2783.
19 G. Wang, H. Liu, J. Liu, S. Qiao, G. M. Lu, P. Munroe and H. Ahn, Adv. Mater., 2010, 22, 4944.
20 D. Wang, D. Choi, Z. Yang, V. V. Viswanathan, Z. Nie, C. Wang, Y. Song, J.-G. Zhang and J. Liu, Chem. Mater., 2008, 20, 3435.
21 H. Zhou, D. Li, M. Hibino and I. Honma, Angew. Chem., Int.Ed., 2005, 44, 797.
22 S. K. Das, S. Darmakolla and A. J. Bhattacharyya, J. Mater. Chem., 2010, 20, 1600.
23 K. Wang, M. Wei, M. A. Morris, H. Zhou and J. D. Holmes, Adv. Mater., 2007, 19, 3016.
24 H.-G. Jung, S. W. Oh, J. Ce, N. Jayaprakash and Y.-K. Sun, Electrochem. Commun., 2009, 11, 756.
25 G. F. Ortiz, A. Berenguer-Murcia, M. Cabello, D. Cazorla-Amoros and J. L. Tirado, Electrochim. Acta, 2015, 166, 293.
26 W. Yue, C. Randorn, P. S. Attidekou, Z. Su, J. T. Irvine and W. Zhou, Adv. Funct. Mater., 2009, 19, 2826.
27 M. Zhen, M. Sun, G. Gao, L. Liu, and Z. Zhou, Chem. Eur. J. 2015, 21, 5317.
28 K.-H. Lee and S.-W. Song, ACS Appl. Mater. Interfaces, 2011, 3, 3697.
29 Y. B. Liu, T. B. Lan, W. F. Zhang, X. K. Ding and M. D. Wei, J. Mater. Chem. A, 2014, 2, 20133.
30 J. Wang, Y. Zhou, Y. Hu, R. O'Hayre, and Z. Shao, J. Phys. Chem. C, 2011, 115, 2529.
31 H. Geng, H. Ming, D. Ge, J. Zheng and H. Gu, Electrochim. Acta, 2015, 157, 1.
32 P. Wang, J. Lang, D. Liu and X. Yan, Chem. Commun., 2015, 51, 11370.
33 X. Xin, X. Zhou, J. Wu, X. Yao, and Z. Liu, ACS Nano, 2012, 6, 11035.
34 H.-C. Tao, L.-Z. Fan, X. Yan, and X. Qu, Electrochim. Acta, 2012, 69, 328.
35 M. M. Zhen, S. Q. Guo, G. D. Gao, Z. Zhou and L. Liu, Chem. Commun., 2015, 51, 507.
36 V. Etacheri, J. E. Yourey and B. N. Bartlett, ACS Nano, 2014, 8, 1491.
37 Q. Q. Zhang, R. Li, M. M. Zhang, B. L. Zhang and X. L. Gou, J. Energy Chem., 2014, 23, 403.
38 X. Yan, Y. J. Li, F. Du, K. Zhu, Y. Q. Zhang, A. Y. Su, G. Chen and Y. J. Wei, Nanoscale, 2014, 6, 4108.
39 J. S. Chen, Z. Wang, X. C. Dong, P. Chen and X. W. Lou, Nanoscale, 2011, 3, 2158.
40 Y. Xu, H. Bai, G. Lu, C. Li and G. Shi, J. Am. Chem. Soc., 2008, 130, 5856.
41 C. S. Rout, B.-H. Kim, X. D. Xu, J. Yang, H. Y. Jeong, D. Odkhuu, N. Park, J. Cho and H. S. Shin, J. Am. Chem. Soc., 2013, 135, 8720.
42 D. H. Chen, L. Cao, F. Z. Huang, P. Imperia, Y.-B. Cheng and R. A. Caruso, J. Am. Chem. Soc., 2010, 132, 4438.
43 W. Li, J. Yang, Z. Wu, J. Wang, B. Li, S. Feng, Y. Deng, F. Zhang and D. Zhao, J. Am. Chem. Soc., 2012, 134, 11864.
44 D. R. Dreyer, S. Park, C. W. Bielawski and R. S. Ruoff, Chem. Soc. Rev., 2010, 39, 228.
45 Y. Zhu, S. Murali, W. Cai, X. Li, J. W. Suk, J. R. Potts and R. S. Ruoff, Adv. Mater., 2010, 22, 3906.
46 C. Z. Zhu, S. J. Guo, Y. X. Fang and S. J. Dong, ACS Nano, 2010, 4, 2429.
47 B. C. Qiu, M. Y. Xing and J. L. Zhang, J. Am. Chem. Soc., 2014, 136, 5852.
48 H. Cao, B. Li, J. Zhang, F. Lian, X. Kong and M. Qu, J. Mater.Chem., 2012, 22, 9759.
49 S. X. Yu, L. W. Yang, Y. Tian, P. Yang, F. Jiang, S. W. Hu, X. L. Wei and J. X. Zhong, J. Mater. Chem. A, 2013, 1, 12750.
50 Y. Qiao, X. L. Hu, Y. Liu, C. J. Chen, H. H. Xu, D. F. Hou, P. Hu and Y. H. Huang, J. Mater. Chem. A, 2013, 1, 10375.
51 S. J. Ding, J. S. Chen, D. Y. Luan, F. Y. Chiang Boey, S. Madhavibc and X. W. Lou, Chem. Commun., 2011, 47, 5780.

52 J. S. Chen, Y. L. Tan, C. M. Li, Y. L. Cheah, D. Y. Luan, S. Madhavi, F. Y. C. Boey, L. A. Archer and X. W. Lou, J. Am. Chem. Soc., 2010, 132, 6124.
53 R. W. Mo, Z. Y. Lei, K. N. Sun and D. Rooney, Adv. Mater., 2014, 26, 2084.
54 W. Li, F. Wang, S. S. Feng, J. X. Wang, Z. K. Sun, B. Li, Y. H. Li, J. P. Yang, A. A. Elzatahry, Y. Y. Xia and D. Y. Zhao, J. Am. Chem. Soc., 2013, 135, 18300.
55 J. Y. Shin, D. Samuelis and J. Maier, Adv. Funct. Mater., 2011, 21, 3464.